Comparative Analysis of Direct Method and Fast Multipole Method for Multirotor Wake Dynamics

B. Sengupta[1]

[1]*Nanyang Technological University, Singapore 639798, Republic of Singapore*

Y. Lee[2],

[2]*Korea Aerospace Industries, Sacheon, Gyeongnam 52529, South Korea*

M. S. Araghizadeh[3], R. S. Myong[3], H. Lee[3*]

[3]*Gyeongsang National University, Jinju, Gyeongnam 52828, South Korea*

Abstract

The rapid growth of urban air mobility (UAM) and electric vertical take-off and landing (eVTOL) aircraft has spurred the demand for designing efficient next-generation urban transport. Distributed electric propulsion (DEP) systems, employing multiple lifting rotors or prop-rotors, offer promising solutions for eVTOL aircraft. However, accurately simulating the complex wake flow resulting from rotor interactions poses significant computational challenges. This study aims to compare the feasibility and effectiveness of the direct method and fast multipole method (FMM) in predicting wake geometry and vortical structures. Vortex particle method (VPM) simulations utilizing both methods are conducted on various rotor models, analyzing key parameters such as tip vortex trajectory, wake geometry, vortical structures, and wake-induced downwash. The findings highlight the effectiveness of FMM in accurately capturing the intricate wake flow of isolated- and multi-rotor systems by comparing the computational times. This study contributes to the comprehensive understanding of wake dynamics and rotor aerodynamics, providing valuable insights for design engineers. Additionally, simulations of multirotor systems in hover and forward flight conditions demonstrate the feasibility of employing VPM with FMM in realistic operational conditions.

Keywords: Vortex Particle Method (VPM), Fast Multipole Method (FMM), Nonlinear Vortex Lattice Method (NVLM), Vortex Methods, Wake Dynamics, Multirotor

---

[*] Corresponding author's e-mail: hlee@gnu.ac.kr

1. Introduction

The need for more efficient rotorcraft led to an effort to develop the technologies of urban air mobility (UAM) and electric vertical take-off and landing (eVTOL) aircraft. The versatility, VTOL capability, and maneuverability of rotorcraft make them excellent candidates for next-generation urban transport systems in highly populated areas [1,2]. Advances in the efficiency of electric propulsion, particularly in areas of motor and battery technologies, enable engineers to employ multiple lifting rotors or prop-rotors for novel designs of eVTOL aircraft. However, the new configurations based on distributed electric propulsion (DEP) systems give rise to complicated interactional problems, which create more numerical and physical challenges to simulate the rotor wake flow accurately and efficiently.

Strong interactions within the wakefields of VTOL aircraft directly impact vehicle performance [3], vibration [4], maneuverability [5,6], and noise [7,8]. The dominant vortical structure of the rotor wake involves tip vortices evolving from blade tips. Recent studies have indicated that tip vortices play key roles in both acoustics and aerodynamics of UAM aircraft [9–11]. To date, accurately predicting tip vortices evolving from blades has been one of the most challenging tasks since these concentrated vortices are intrinsically unsteady and vulnerable to disturbance. Although experimental [12–14] and high-fidelity computational fluid dynamics (CFD) [15–19] approaches have been used to analyze complex wake dynamics, high consumption of time and resources makes these methods unfeasible for studying the emerging category of eVTOLs, particularly in the initial design stages [20,21]. With the increasing number of rotor systems, vortex methods have emerged as useful and popular tools to describe the rotorcraft wake flow and its complex interactional phenomena [22–24]. The numerical dissipation of CFD methods, along with their computational burden, persuades researchers to exploit rather faster vortex approaches, like the free-wake method (FWM) and vortex particle method (VPM) [25,26], to study the wakefield.

In the FWM, the rotor wake sheet is divided into trailing and shed vortices. The strength of a trailing vortex is the radial change between the bound vortices, whereas the strength of a shed vortex is related to the azimuthal change in the bound vortices with time [27,28]. The time-marching free-wake method allows the vortex sheet, consisting of vortex filaments shed from the rotating blade, to move freely as the wake propagates downstream. Since the FWM fundamentally exploits empirical data to consider the effects of turbulence on the diffusive characteristics of vorticity and vortex stretching [29], the simulation results strongly depend on the empirical parameters. Furthermore, the FWM requires that connectivity among vortex elements be preserved strongly, and this causes additional difficulty during

interaction between wake vortices and body surfaces. In the VPM, the rotor wake generated from the trailing edge of the blade is modeled by a number of distinct vortex particles, which interactionally affect each other's velocity and location within the wakefield. Therefore, unlike the vortex filament method, VPM has the advantage that the particles do not necessarily need to maintain connectivity with adjacent particles because particles propagate independently during the time-marching step. This feature is especially useful for evaluating wake flow interactional phenomena. Moreover, the vorticity-velocity form of the incompressible Navier-Stokes equations is solved with a Lagrangian description to obtain the wake vorticity field. Therefore, VPM can consider the viscous effects and avoid artificial numerical dissipation.

While flow is passing over the rotor blade, vortex particles keep emitting from it, and the number of particles increases at every time step. Although the number of wake elements determines the accuracy of the wake region prediction, the increase in the number of vortex particles extends the computational time of the numerical simulation [30,31]. Compared to traditional flight vehicles, eVTOL and UAM aircraft are equipped with DEP systems based on multiple lifting rotors or prop-rotors, which expand the number of vortex particles exponentially, thus leading to an N-body problem with time complexity of $O(N^2)$ for VPM simulation. Here N is the number of vortex particles. The computational cost of direct evaluation for N number of particles could be prohibitive. Consequently, evaluation of the wake-induced velocity of each particle can be a bottleneck of the whole process of rotor simulations, degrading the advantage of utilizing mid-fidelity methods. There are some trustworthy alternative algorithms to the direct method that could improve the scalability of particle-based models. The bedrock of these algorithms is to decompose the wake domain into distinct clusters of particles and then calculate the interactional effect between the distinct and far clusters, and finally apply cluster evaluation to the particles. One such algorithm is the hierarchical tree method [32], which reduces the order of the N-body problem to $O(N \times logN)$ [33–35]. The other way is the fast multipole method (FMM) [36]. The FMM [37–40] is able to reduce the computational cost of the problem roughly to $O(N)$ and, in ideal cases, even to $O(N)$.

Previous researchers have focused on efficient computation by FMM; their work has led to the introduction of various kinds of algorithms within the FMM family, with the utilization of various options with hardware architectures in the field of rotor aerodynamics. Deng et al. [41] introduced the dipole panel fast multipole method (DPFMM), which provided a rapid evaluation of the induced velocity in the unsteady vortex lattice method (UVLM). With approximately the same precision as the direct method, the Biot-Savart kernel method was used to calculate the

multipole expansion coefficients of a quadrilateral dipole panel in spherical coordinates. Thönnißen et al. [42] proposed the vortex pseudo-particle method (VPPM), which has the advantage of simple implementation compared to conventional FMM, without need for imposition of boundary condition, and which provided the time complexity of $O(N \times logN)$. Vines et al. [43] developed a coupled method to solve flow around solid objects using Lagrangian vortex particles. A variant of FMM known as the black box FMM [44] was used to compute the time evolution of vortex particles. Garrel et al. [45,46] utilized the multi-level multi-integration technique as a fast summation algorithm to predict the rotor aerodynamic quantities. The growing interest in designing new types of eVTOL and UAM aircraft has motivated several research groups to employ VPM simulation with FMM. Previous studies have shown that FMM is an efficient way to alleviate the considerable computational burden of simulating rotor wake flows via modeling of a set of individual vortex particles; potential applications include modeling of helicopter rotors in hover and forward flight [47], comprehensive rotor analysis [48], UAM propeller [49], interaction between rotor and ship deck [50,51], and rotor ground effects [52,53].

Although FMM is a computationally efficient method, predictions of wake geometry and vortical structures behind the rotor disk can be slightly different from results of the direct method due to multipole expansion. Accurately predicting the convoluted wake structure is important in any investigation of the mutual interaction of the wake flow with rotating blades, which interaction has a significant impact on the blade airloads, structural deformation, acoustics, and vibration [54–56]. However, most previous studies have focused on developing efficient and fast summation algorithms that can be utilized to computationally accelerate rotor simulations, and relatively little research has presented differences in the evolution of the wake geometry and vortical structures predicted by direct method and FMM. From the above literature, major gaps from work reported on VPM simulations with FMM are summarized in two areas. First, differences in wake characteristics of rotor blades as computed by direct method and FMM are explored in terms of tip vortex trajectory, wake geometry, vortical structures, and wake-induced downwash. Second, time profiling for total simulations by direct method and FMM until stabilization of thrust coefficient with respect to number of revolutions and vortex particles is addressed, which will be beneficial for design engineers. In this study, VPM simulations using the direct method and FMM are applied to simulate the evolution of wake structures of two different rotors in hover: (1) a Caradonna-Tung rotor model to compare the aerodynamic forces and tip vortex trajectory in terms of radial and axial positions [57], and (2) an OH-13E rotor model to compare wake-induced downwash and vortical structures [58]. Results of FMM-based simulation are compared against predictions from the

direct method and the experimental data, and a discussion of associated wake dynamics and rotor aerodynamics is presented. Finally, a multirotor operating in hover and forward flight conditions is simulated using the VPM with the direct method and FMM. The two predictions of the evolution of wake-induced downwash and vortical structures containing strong wake interaction phenomena are compared; results show the feasibility and effectiveness of VPM with FMM at simulating eVTOL and UAM aircraft with DEP systems based on multiple lifting rotors or prop-rotors.

2. Numerical Methods

2.1 Vortex Particle Method

The FWM and VPM are widely used to represent the vorticity field in the rotor wake. The vortex filament is treated as concentrated vortices along a segment with a singularity at the center, whereas the vortex particles are modeled as concentrated vortices within a volume. Compared to the straight or curved vortex filament approaches, the VPM has the advantage of not requiring particles to maintain connectivity with adjacent particles because individual particles can be transported independently during the time-marching simulation. This characteristic is particularly relevant when examining the effects of wake interaction with rotors or rotor-fuselage configurations. The vortex particles forming the wake structure interact with each other and are permitted to move freely downstream with local convection velocity.

In the present work, the rotor wake is shed from the full span of the rotor blade; it is modeled using a finite number of vortex particles. The strength of each particle is determined by applying the Kutta condition to the vortex elements placed on the trailing edge, where their strength is computed from the simulation of the nonlinear vortex lattice method (VLM) developed by the authors [59–62]. The vorticity field can be formulated by a set of N Lagrangian vector-valued particles, as follows:

$$\boldsymbol{\omega}(\mathbf{x},t) = \sum_{i=1}^{N} \boldsymbol{\alpha}_i(t)\, \zeta_\sigma\left(\mathbf{x} - \mathbf{x}_i(t)\right) \tag{1}$$

$$\boldsymbol{\alpha}_i(t) = V_i\, \boldsymbol{\omega}_i(\mathbf{x}_i, t) \tag{2}$$

Here, $\boldsymbol{\omega}(\mathbf{x}, t)$ indicates the vorticity field in the wake, and $\boldsymbol{\alpha}(t)$ implies the strength vector, where $\mathbf{x}$ is the position vector of an arbitrary point in the field. V_i and $\mathbf{x}_i$ are the volume and the position vector of the i-th vortex particle, respectively. In addition, $\mathbf{r}$ is the position vector between $\mathbf{x}$ and $\mathbf{x}_i$.

$$\zeta_\sigma(\mathbf{r}) = \sigma^{-3}\zeta\left(\frac{|\mathbf{r}|}{\sigma}\right) \tag{3}$$

$$\zeta(\rho) = \frac{1}{(2\pi)^{3/2}}e^{-\rho^2/2} \tag{4}$$

$\zeta_\sigma(\rho)$ is the three-dimensional regularization function, and σ is the smoothing radius, needed to avoid a singularity problem [63]. The smoothing radius in this work is equal to the vortex particle's core radius; the higher-order algebraic smoothing function developed by Winckelmans and Leonard is used to represent the vorticity distribution near the vortex particles [63,64]. The wake-induced velocity can be calculated in discretized form from the particle representation of the vorticity fields, as follows:

$$\mathbf{u}(\mathbf{x},t) = \sum_{i=1}^{N}\mathbf{K}_\sigma\left(\mathbf{x}-\mathbf{x}_i(t)\right)\times\boldsymbol{\alpha}_i(t) \tag{5}$$

$$\mathbf{K}_\sigma(\mathbf{r}) = -\left(\frac{q_\sigma(\mathbf{r})}{|\mathbf{r}|^3}\right)\mathbf{r} \tag{6}$$

$$q_\sigma(\mathbf{r}) = q\left(\frac{|\mathbf{r}|}{\sigma}\right) \tag{7}$$

Here, $\mathbf{K}_\sigma(\mathbf{r})$ is the regularized Biot-Savart kernel and $q_\sigma(\mathbf{r})$ is an integration of the smoothing function. The three-dimensional high-order algebraic smoothing function, $q(\mathbf{r})$, becomes:

$$q(\rho) = \frac{1}{4\pi}\frac{\rho^3\left(\rho^2+5/2\right)}{\left(\rho^2+1\right)^{5/2}} \tag{8}$$

For a time-marching rotor simulation, the vortex particle's local convection velocity, which is a sum of the freestream velocity, the velocity induced by the rotor blade, and the wake-induced velocity, will be iteratively evaluated to update the location of the particles during the numerical time integration. The calculation of the wake-induced velocity from the vortex particles can be performed directly using the Biot-Savart law. A set of N vortex particles is given with their positions $\mathbf{x}_i \in \mathbf{R}^3$; then, calculation of the wake-induced velocity for all particles requires $O(N^2)$, known as the N-body problem, since the vortex particles influence each other.

6

2.2 Kernel independent FMM

Fast summation algorithms can be divided into three categories: (1) fast multipole methods, (2) the tree-code approach, and (3) rapid convolution methods on a regular grid. The kernel-independent FMM used in this study is included in the first category, and it becomes possible to achieve efficient three-dimensional expansions [39]. The key feature of the kernel-independent FMM is that it is based solely on kernel evaluations and does not require the implementation of multipole expansions of the underlying kernel. Instead of analytic expansions, a continuous distribution of an equivalent density is employed on a surface encircling the box to describe the potential created by sources inside the box of the hierarchical FMM tree [40,65,66]. Local Dirichlet-type boundary value problems are solved to calculate this equivalent density and match its potential to the potential of the original sources at a surface in the far field. Fast Fourier transforms are also used to sparsify the far-field evaluations. Moreover, implementation of the kernel-independent FMM is relatively simple compared to that of conventional FMM [67,68].

To solve the *N-body problem* using FMM, a tree data structure T is used to partition the domain. The FMM algorithm reduces the time required to $O(N)$. Eq. (5) for computing induced velocity at particle i can be rewritten in matrix form in which $\left[\tilde{\boldsymbol{\alpha}}_j\right]$ is the skew-symmetric matrix spanned by the vector $\boldsymbol{\alpha}_j$ [69]:

$$\mathbf{u}\left(\mathbf{x}_i, t\right) = \sum_{j=1}^{N}\left[\tilde{\boldsymbol{\alpha}}_j\right]\mathbf{K}_\sigma\left(\mathbf{x}_i - \mathbf{x}_j\right) \tag{9}$$

Then, the interactions are computed from all other tree nodes in T for each target point $\mathbf{x}_i$ in tree node B. These interactions are divided into two categories in FMM, near interactions and far interactions, as expressed in Eq. (10):

$$\mathbf{u}\left(\mathbf{x}_i, t\right) = \sum_{\mathbf{x}_j \in N(B)}\left[\tilde{\boldsymbol{\alpha}}_j\right]\mathbf{K}_\sigma\left(\mathbf{x}_i - \mathbf{x}_j\right) + \sum_{\mathbf{x}_j \in F(B)}\left[\tilde{\boldsymbol{\alpha}}_j\right]\mathbf{K}_\sigma\left(\mathbf{x}_i - \mathbf{x}_j\right) \tag{10}$$

Near interactions are calculated by direct summation, which involves summing contributions from each source point $\mathbf{x}_j \in N(B)$. The tree nodes that are farthest from B are referred to as *well-separated* ($\mathbf{x}_j \in F(B)$) from B. Interactions from source points in a well-separated tree node to target points in B are low-rank and can be approximated. Moreover, far-field interactions in FMM are computed hierarchically at the coarsest possible length scale rather than at the leaf level. Interactions with target node B are computed from other source nodes B_S that are not well-separated from $P(B)$ (parent of B) at the finest level. Similarly, interactions with $P(B)$ are computed from source nodes B_S ,

and so on for all ancestors of B at a coarser level. Finally, all of B's ancestors' contributions are added to derive the far-field potential at target places in B.

The key features of kernel Independent FMM are summarized here. The far-field translation operator, which is the fundamental feature of KIFMM, along with the multipole and local expansions, two essential building blocks for FMM in the context of KIFMM, are discussed [68,70]. Lastly, far-field interactions will be defined by translation operators between these expansions.

2.2.1. Multipole Expansion

The multipole expansion approximates the far-field potential due to the source points within B for a tree node B. The potential $\mathbf{u}^{u,B}$ is evaluated from these source points at points $\mathbf{x}_j^{u,B}$ on a check surface, as represented in Eq. (11). After that, a linear system is solved to compute a set of densities $\boldsymbol{\alpha}^{u,B}$ for points $\mathbf{x}_j^{u,B}$ on an equivalent surface [68].

$$\mathbf{u}^{u,B}\left(\mathbf{x}_i,t\right)=\sum_{\mathbf{x}_j\in B}\left[\tilde{\boldsymbol{\alpha}}_j\right]\mathbf{K}_\sigma\left(\mathbf{x}_i^{u,B}-\mathbf{x}_j\right),\ \forall i \tag{11}$$

Then, by estimating the potential owing to these equivalent sources, the potential at a position well distant from B can be calculated. The points $\mathbf{x}_j^{u,B}$ and $\mathbf{x}_i^{u,B}$ on cubic surfaces (equivalent and check surfaces) centered on B are organized in regular grids in 3D. Each face of the cube has $m \times m$ points, where m is the multipole order, which defines the accuracy of the multipole expansion. The edge lengths of the equivalent surface (s_e) and check surface (s_c) must satisfy the relation $s < s_e < s_c < 3s$, where s is the edge length of B.

2.2.2. Local Expansion

Because the source points are well-separated from a tree node B, the local expansion approximates the potential at points in the interior of B. At points $\mathbf{x}_i^{d,B}$ on a check surface, the potential $\mathbf{u}^{d,B}$ is evaluated from well-separated source points, as defined in Eq. (12). After that, a linear system is solved to compute a collection of densities $\boldsymbol{\alpha}^{d,B}$ for points $\mathbf{x}_j^{d,B}$ on an equivalent surface [68].

$$\mathbf{u}^{d,B}\left(\mathbf{x}_i,t\right)=\sum_{\mathbf{x}_j\in B}\left[\tilde{\boldsymbol{\alpha}}_j\right]\mathbf{K}_\sigma\left(\mathbf{x}_i^{d,B}-\mathbf{x}_j\right),\ \forall i \tag{12}$$

Then, by computing the potential owing to these equivalent sources, the potential at a point in the interior of B can be calculated. For multipole expansion, points $\mathbf{x}_j^{d,B}$ and $\mathbf{x}_i^{d,B}$ are organized in regular grids on cubic surfaces (equivalent and check surfaces) cantered on B, with $m \times m$ points on each face. The edge lengths of the equivalent surface (s_e) and check surface (s_c) must satisfy the relation $s < s_e < s_c < 3s$, where s is the edge length of B [68].

2.2.3. Tree construction

The continuous source distribution f is discretized using a piecewise polynomial representation. An octree is utilized to discretize the domain and Chebyshev polynomials at each leaf node. The given density function f is assessed at the Chebyshev nodes in each leaf node; then, using a tensor product algorithm, the Chebyshev coefficients are computed and coefficients up to degree q are kept. The function f can now be evaluated at a position (x_1, x_2, x_3) for each leaf node using Eq. (13):

$$f(x_1, x_2, x_3) = \sum_{i,j,k \geq 0}^{i+j+k \leq q} \alpha_{i,j,k} T_i(x_1) T_j(x_2) T_k(x_3) \tag{13}$$

where $\alpha_{i,j,k}$ are the Chebyshev coefficients and $T_i(x_1)$ is the Chebyshev polynomial of degree i in x. In adaptive mesh refining, initialization with a uniform octree and the absolute sum of the highest order coefficients are computed for each tree node. For each node, this yields an estimate of the polynomial truncation error. The tree nodes are progressively split with a truncation error greater than a specified tolerance ε_{tree} until the desired tolerance or the maximum allowable depth for the tree is reached.

3. Prediction of tip vortex trajectories

3.1 Caradonna-Tung rotor model

Experiments using the Caradonna-Tung rotor model [57] provided extensive measurements of rotor aerodynamics and wake dynamics, which have been widely utilized for validating the capability of the wake model of reproducing the tip vortex trajectories as a function of wake ages. The Caradonna-Tung rotor has two NACA 0012 blades mounted on a tall column with a rectangular planform. The rotor blade's aspect ratio is 6, the chord length is 0.1905m (0.625 ft), and the rotor diameter is 2.286m (7.5 ft), as listed in Table 1. Under well-controlled environments, a wide range of test settings was examined, with a tip Mach number ranging from 0.226 to 0.890 and a collective pitch angle ranging

from 0 to 12 degrees. After recording pressure distributions at five cross-sections of the blade, the tip vortex trajectory was recovered using a hotwire technique. The flow conditions used in this study are listed in Table 2.

Table 1 Model description of Caradonna-Tung rotor [57]

Parameter	Value
Number of blades, N_B [-]	2
Chord length, c [m]	0.1905
Rotor radius, R [m]	1.143
Twist angle, θ_{twist} [deg.]	0
Blade planform	Rectangular blade
Blade sectional profile	NACA 0012 airfoil

Table 2 Flow conditions of Caradonna-Tung rotor simulation

Parameter	Value
Collective pitch angle, θ_c [deg.]	5, 8, 12
Rotating speed, Ω [rpm]	1250
Tip Mach number, M_{tip} [-]	0.439

3.2 Aerodynamic forces and tip vortex trajectories

The thrust coefficient is a non-dimensionalized representation of the aerodynamic load given to the rotor blades in a direction normal to the rotating plane. We performed multipole order independence studies and observed that multipoles of order above 6 had no significant effect on the results [71]. Moreover, the aim of employing FMM is to yield efficient computation with respect to computational time and resources with adequate accuracy. Therefore, all the simulations were performed with a multipole of order 6. A comparison between FMM and the direct method for the integrated thrust coefficient with respect to the collective pitch angle (θ_c) of the rotor blade is shown in Fig. 1. Here, FMM and direct simulation are illustrated by the dashed blue line with circle symbols and the red dashed line with plus symbols, respectively; these can be compared with the experimental data, depicted by the scattered black circle. With increases in pitch angle, the thrust force on the rotor increases. Values of integrated thrust coefficient,

obtained by FMM method for each of the collective pitch angles, are very similar, with slight over-prediction compared to those values obtained from the direct method, as shown in Fig. 1. Each revolution of the rotor is divided into 72 (for $\Delta\psi = 5^o$) divisions. Since FMM is an approximate method and these approximations are summed up based on the number of divisions per revolution and the total number of revolutions, the FMM results deviate from the results obtained by the direct method.
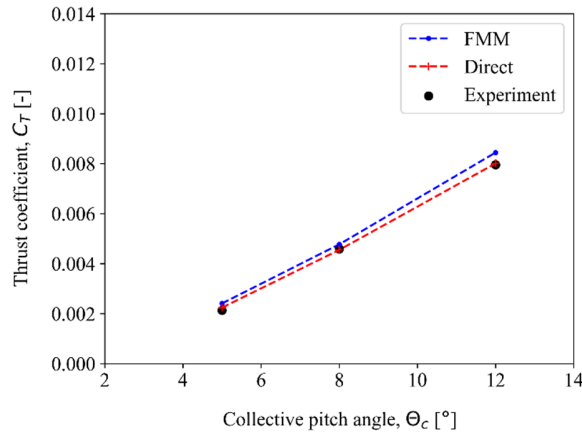
Fig. 1 Comparison of integrated thrust coefficients at pitch angles of 5º, 8º, and 12º.

(a) Collective picth angle (θ_c) of 5º
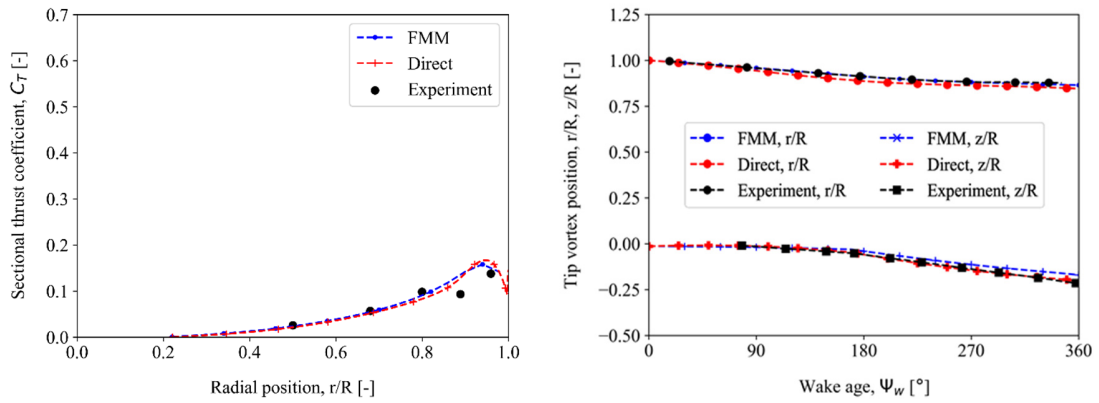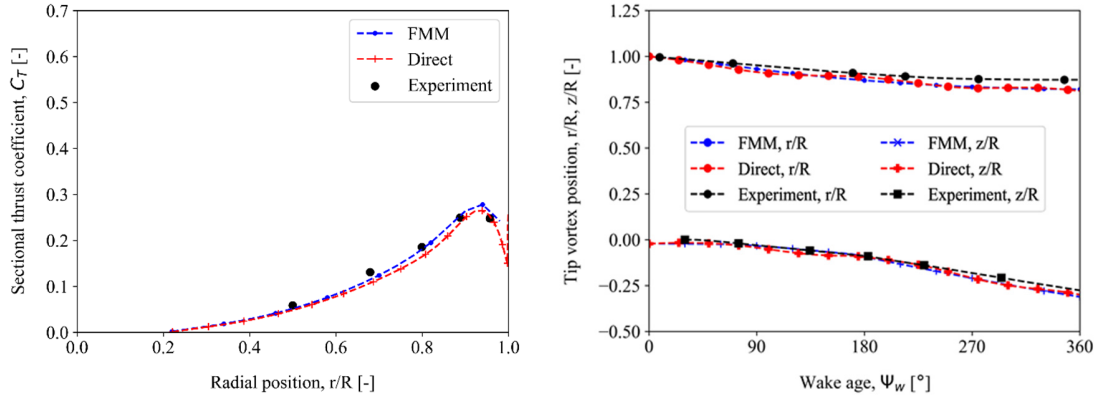
(b) Collective picth angle (θ_c) of 8°
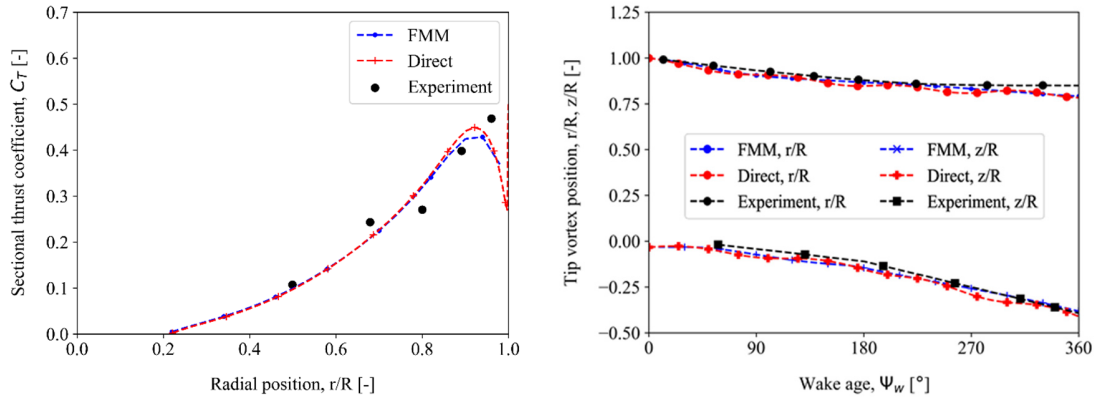
(c) Collective picth angle (θ_c) of 12°

Fig. 2 Comparison of sectional thrust coefficients (left) and tip vortex trajectories (right) for various pitch angles.

Figure 2 (left) shows a comparison of the sectional thrust coefficient along the radial direction between FMM and direct method; the results were validated against those of the experiment for various pitch angles, as can be seen in Table 2. The quantities obtained by FMM methodology are illustrated by a blue dashed line with circle symbols; a red dashed line with plus symbols was employed for direct, whereas scattered black dot represents the experimental quantities. The same notations used in Fig. 1 are preserved throughout the article, except for the tip vortex trajectory (Fig. 2 (right)). It was observed that the sectional thrust coefficient distribution along the radial direction of the blade, obtained by FMM simulation, agrees well in all cases with the direct simulation results as well as with the experimental values.

Tip vortices are generated due to the pressure difference between the upper side (low pressure) and lower side (high pressure) at the tip location of the rotor blade. The spiral pattern of the tip vortices during hovering can be observed due to the resultant velocity of the rotor motion and tip vortex velocity. A comparison of tip vortex trajectory locus for different collective pitch angles, namely 5°, 8°, and 12°, is shown in Fig. 2 (right). The locus of a particular tip vortex is tracked within a rotor revolution. The locus is described by non-dimensionalized radial and downwash direction with respect to azimuthal angles. The experimental locus of the tip vortex is represented by the scattered circles and square symbols for radial and axial directions, respectively. Similarly, results obtained from FMM computation in the radial and axial directions are represented by dashed blue lines with circle and square symbols, respectively; for the direct simulation, red dashed lines with plus and cross symbols were used. We observed that the tip vortex trajectory obtained from FMM simulations showed excellent agreement with the direct method and experimental results in all cases with different collective pitch angles.

3.3 Wake structure and vorticity field

The rotor wake is defined as an unsteady fluctuation flow that induces unsteady rotor blade aerodynamics, adding more complication to the flow field. Lagrangian-based vortex particles were employed to depict the wake arising from the entire span of the rotor blades. The evolution of wake geometries of the Caradonna Tung rotor for both FMM (top) and direct (bottom) with respect to revolutions for a collective pitch angle of 8° are shown in Fig. 3. The size of the wake vortex particles is determined by the associated circulation strength: the larger the particle size, the stronger the wake vortex strength. The color of the vortex particles, like their size, varies with their circulation strength. The development of near and far wakes was computed as the rotor revolutions increased; tip vortex descent and wake contraction, which can be clearly noticed in both types of computation, are the key features in the rotor wakefield. We observed that the wake structure near the rotor blade is similar in both FMM and direct simulations. However, the wake structure after the contraction of the wake has some dissimilarities from observable wake distortion. This may be because, as the number of revolutions of the rotor progresses, the error in the FMM gets integrated and generates a slightly dissimilar wake structure after contraction. It is important to note that slight dissimilarities arise only after a considerable number of rotor revolutions. Still, the dissimilarities in wake structure, as explained, do not affect the overall prediction, as illustrated in Figs. 2 and 3.

(a) 5 rev.   **(b) 10 rev.**   **(c) 15 rev.**
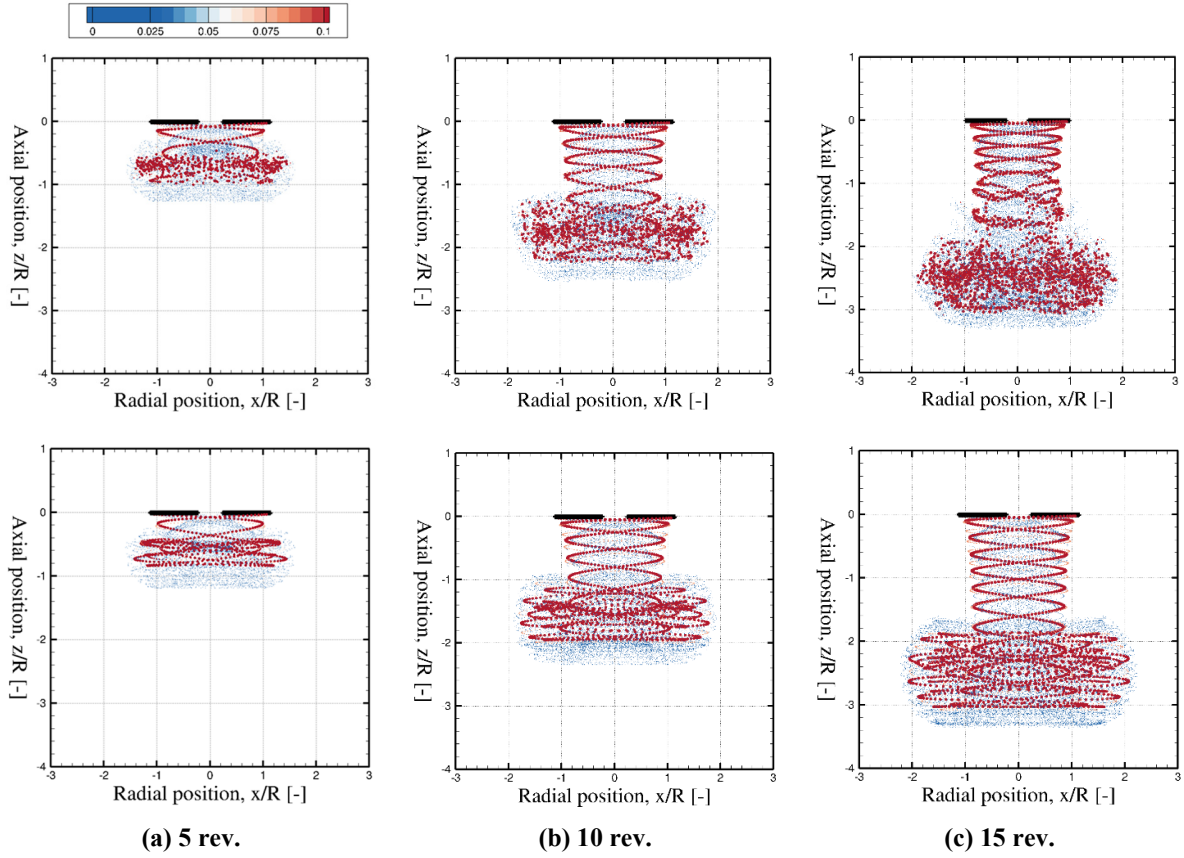
Fig. 3 Comparison of evolution of wake structures predicted by VPM with FMM (top) and direct (bottom) methods.

The evolution of unsteady wake geometries behind the rotor with the aid of the vorticity fields is described in Fig. 4. The contours of vorticity magnitude on a vertical cross-section (x–z plane) across the center of the rotating axis were compared for FMM and direct simulations with the increase in revolutions. The vorticity contour plots show clear evidence of periodic shedding of wake vortices behind the rotor plane in both circumstances. In the wake vortices, different colors indicate opposing directions of vorticity. Individual plots in the figure show the vortex structures, which are mostly made up of tip vortices and shear layers. The pressure differential at the blade tip generates pairs of tip vortices, while shear layers are formed by merging of boundary layers on the upper and lower sides of the blade [72]. Although all the features of the wake were captured properly, there are small differences in the magnitude of the vorticity contours with the loss of symmetry, especially at higher revolutions, as can be seen in Fig. 4 (c).

14

(a) 5 rev.   **(b) 10 rev.**   **(c) 15 rev.**
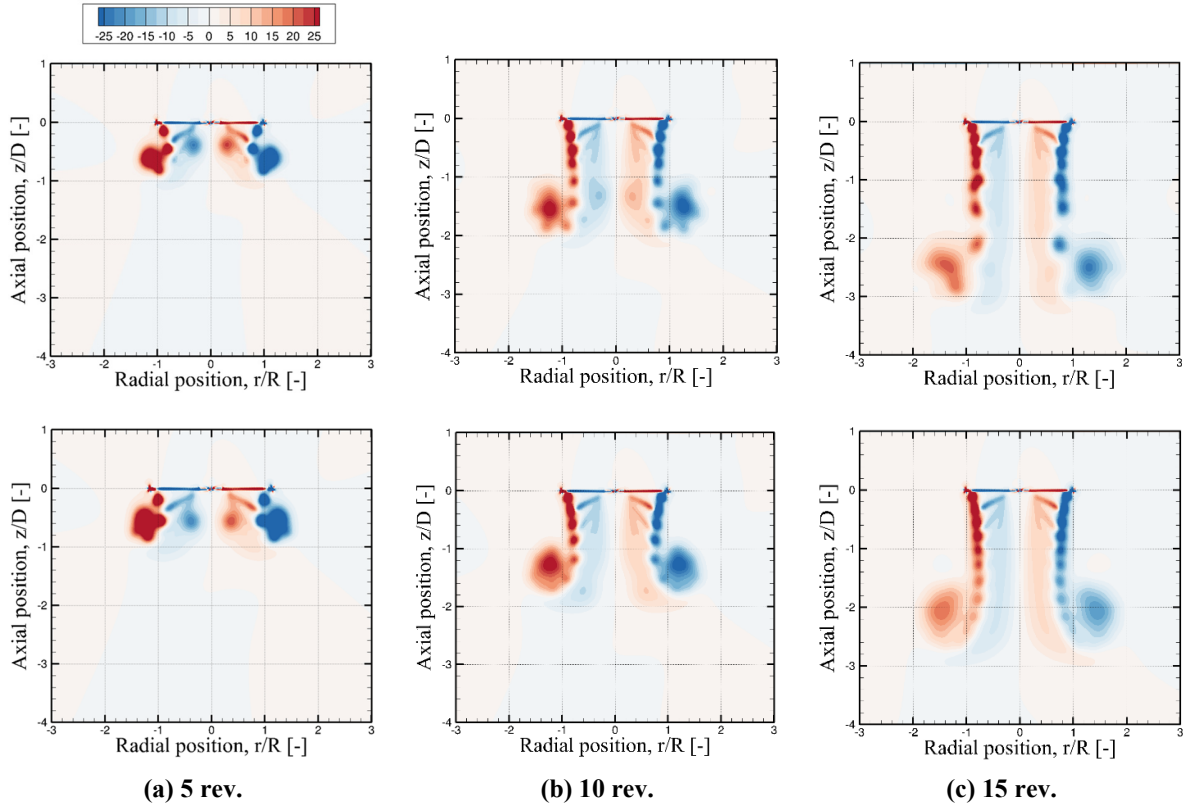
Fig. 4 Comparison of evolution of vortical structures predicted by VPM with FMM (top) and direct (bottom) methods.

Comparison of time profiling for the case with a collective pitch angle of 8º was chosen, with the same computational resources as shown in Fig. 5. It was observed that with a lower number of particles, the direct method consumes less time than does the FMM method; however, the computational time increases exponentially for the direct method with increases in number of particles. However, it is interesting to note that despite increases in number of particles, the increase in time for FMM computation is very low. This is because the algorithm of FMM involves a number of operations that remain the same regardless of the number of particles, which makes the method less efficient at lower numbers of particles; however, with its resources for higher numbers of particles, the FMM is not only highly efficient in computational time but also in terms of computational resources.
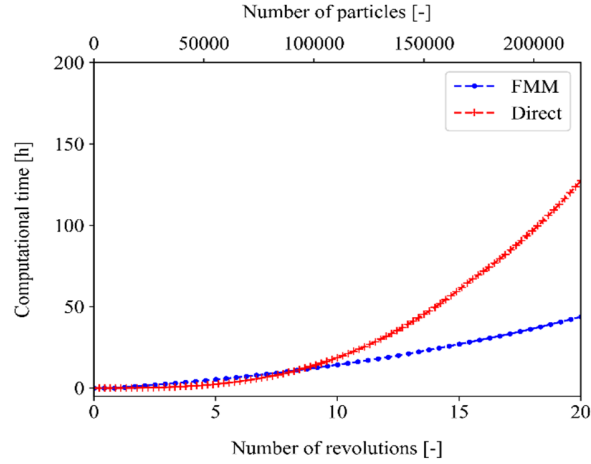
Fig. 5 Comparison of time profiling with respect to number of revolutions for FMM and direct computation

4. Prediction of downwash flow field

4.1 OH-13E rotor model

VPM simulations with FMM and the direct method were applied to predict the wake-induced downwash of a full-scale rotor in hover. The wake-induced velocity is important for determining the evolution of the rotor wake, the induced velocity at the rotor blade, and the surface pressure on the fuselage. In this section, experimental study of the OH-13E rotor model [58] was used to evaluate the numerical results. The OH-13E rotor has two blades with a tapered-twisted planform and NACA 0015 airfoil cross-section. The geometric specifications of the rotor model used for the experiment are given in Table 3. The wake-induced velocities at three different vertical stations downstream of the rotor wake (z = -0.1R, -0.5R, -1.0R; R is the rotor radius and the minus sign indicates a downstream location) were measured using a split-film total-vector anemometer. Data from the anemometer was recorded at blade azimuth angles (ψ) of 0º, 45º, 90º, and 135º; time-averaged results for each station below the rotating plane were used for comparison with VPM simulations. The measurements of the OH-13E rotor model were conducted at two disk-loading conditions and three combinations of blade pitch angle and rotational speed. We chose two conditions in which blade pitch angles at 75% of the span (θ_{75}) were 6.25º and 10.75º, with a fixed tip speed of 137.2 m/s, where the rotor blade generated mean thrust coefficients (C_T) of 0.002 and 0.004, respectively. The predictive capabilities of VPM with FMM and the direct method were evaluated by calculating the integrated thrust coefficients for both conditions prior to comparing the wake-induced downwash flow field. We observed an excellent agreement of the FMM method with the direct

16

method, as well as with experimental values. The discrepancy between FMM and the direct method for blade pitch angles of 6.25º and 10.75º was less than 0.5%, whereas, compared with the experiment, the observed difference was less than 1.0%.

<div align="center">

Table 3 Model description of OH-13E rotor [58]

</div>

Parameter	Value
Number of blades, N_B [-]	2
Root chord length, c_R [m]	0.356
Root chord length, c_T [m]	0.258
Rotor radius, R [m]	5.353
Twist angle, θ_{twist} [deg.]	-4º
Blade planform	Tapered blade
Blade sectional profile	NACA 0015 aerofoil

4.2 Downwash flow field

Correct prediction of downwash velocity is essential in the study of rotor aerodynamics. It is to be noted that, in the present work, the effect of the viscosity of the wake is not considered, which means the strength of the vortex particles will remain constant during wake convection. Experimental data of time-averaged downwash velocity measured at an azimuthal angle of 0º for three vertical stations along the radial direction was chosen for comparison with data from the FMM and direct methods.
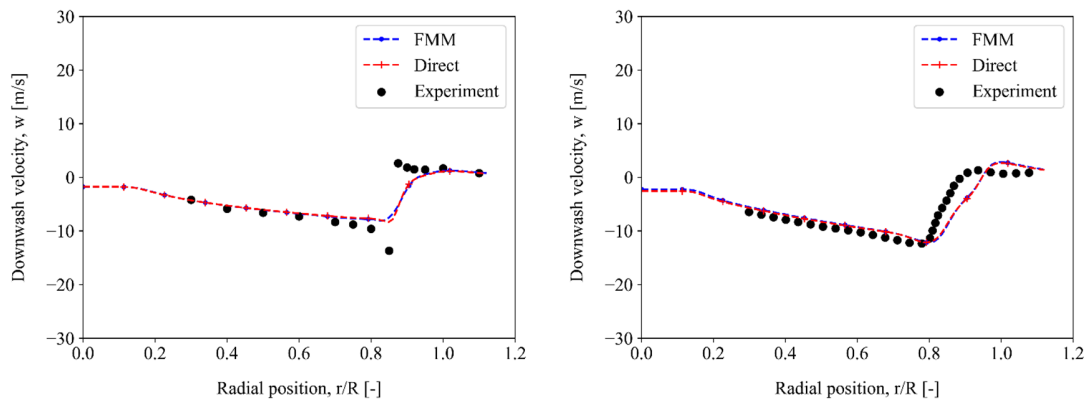
(a) Downstream stations: z = -0.1R
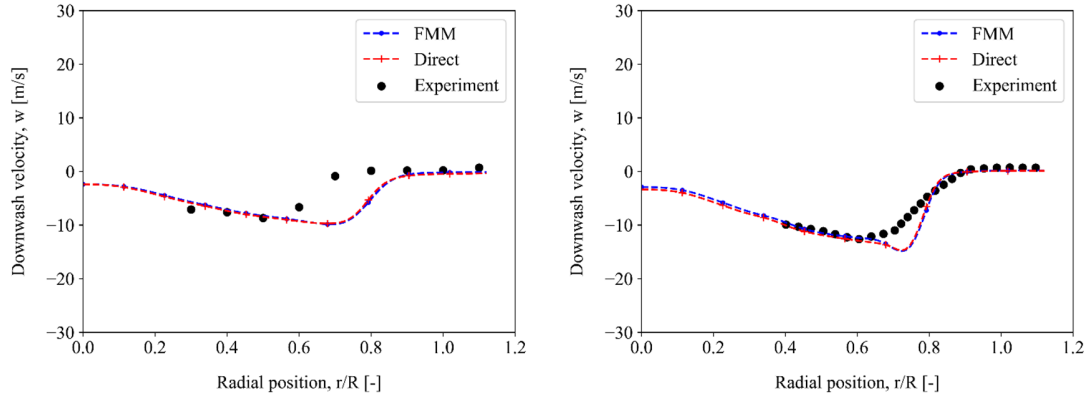
(b) Downstream stations: *z = -0.5R*
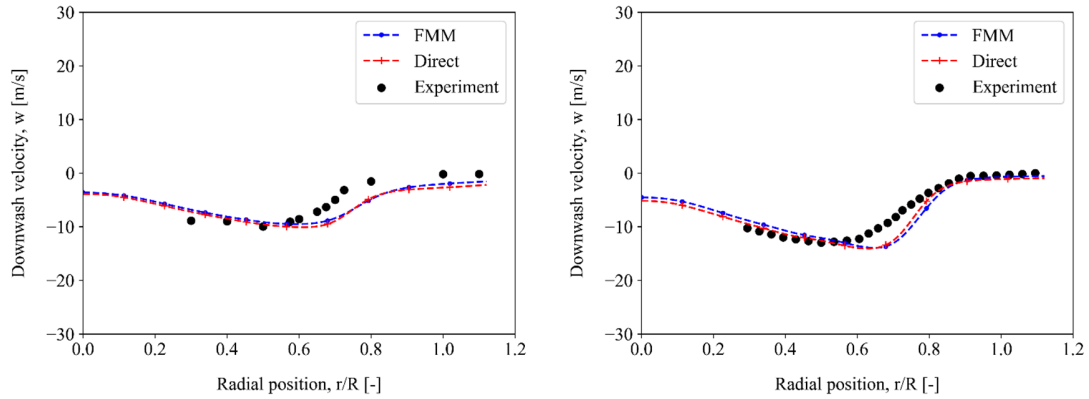
(c) Downstream stations: *z = -1.0R*

Fig. 6 Comparison of predicted downwash with experimental data at collective pitch angles of 6.25º (left) and 10.75º (right).

The time-averaged downwash velocity values along the radial direction for the three locations with pitch angles (θ_{75}) of 6.25º and 10.75º are depicted in Fig. 6. At all the investigated vertical positions, the predicted wake downwash variation for both FMM and direct method matched reasonably well with the experimental data. We thought, however, that if the viscous effect in the wake dynamics had been considered, such consideration would have improved the prediction. The aim of the present study was to observe differences in prediction between FMM and the direct method; therefore, the assumption of inviscid wake convection was sufficient.

According to the measured downwash profile in all the cases (θ_{75} = 6.25º and θ_{75} = 10.75º), the rotor wakes immediately contracts at approximately *r/R = 0.8* after exiting the rotor plane. In the case in which the pitch angle is equal to θ_{75} = 6.25º for the vertical station (*z = -0.1R*), the highest wake contraction was observed in the experiment,

as shown in Fig. 6(a) (left). Although none of the computational methods were able to predict the maximum and minimum values of downwash velocity, the overall distribution was properly captured. Moreover, predictions by FMM and direct method were similar, as illustrated in Fig. 6(a) (left). The vortex particle model was able to reproduce the rapid contraction of the rotor wake, as evidenced by the good agreement at the same vertical station for $\theta_{75} = 10.75^{\circ}$, as shown in Fig. 6(a) (right).

Measurements also revealed that the power of the tip vortex weakened as the wake went downstream, and the wake became more scattered. The phenomenon of wake weakening can be observed in locations downstream ($z = -0.5R$ and $z = -1.0R$). Although the phenomenon of wake weakening was captured, we observed that prediction of downwash velocity at one radial location near $r/R=0.8$ showed some difference compared to the experimental values in the case of $\theta_{75} = 10.75^{\circ}$, although predictions by FMM and direct method were similar, as shown in Fig. 6(b) and 6(c) (right). Similarly, in the case of 6.25° pitch angle (θ_{75}), wake weakening was observed, but wake contraction distribution was different in the prediction compared to the experiment, even though prediction by FMM and direct method were observed to be identical, as illustrated in Fig. 6(b) and 6(c) (left).

Evolution of the wake with respect to revolutions, predicted by FMM and direct methods, is illustrated in Fig. 7. The downwash velocity fields were further provided to explore our understanding of differences due to FMM and the direct method affecting the wake structure; this allowed us to explore the evolution of unstable wake geometries behind the rotor along the induced flow direction. Comparing results of FMM and direct method for contours of downwash velocity on a vertical cross-section (y–z plane) across the center of the rotating axis for the case of $\theta_{75} = 10.75^{\circ}$ showed negligible differences in flow structure (see Fig. 7). Periodical shedding of wake vortices behind the rotor plane was well-captured for all conditions with both FMM and direct method.

The key features of the rotor flowfield, like wake convection and periodic shedding, were predicted well in the FMM simulations. The wake convection distance was observed to be similar to that of the direct method. Another key feature of a hovering rotor is the flow symmetry along the center of rotor rotation. The symmetric profile was captured perfectly by the direct method, as expected, but symmetry was not perfectly conserved in the case of FMM, especially at higher revolutions, as shown in Fig. 7(b) and 7(c). This is evidently because FMM is an approximate method, as explained earlier. It is important to note that the deviation of non-symmetry in the flow field computed by FMM is small, and does not have much effect on the overall prediction.

19

(a) 5 rev.	**(b) 10 rev.**	**(c) 15 rev.**
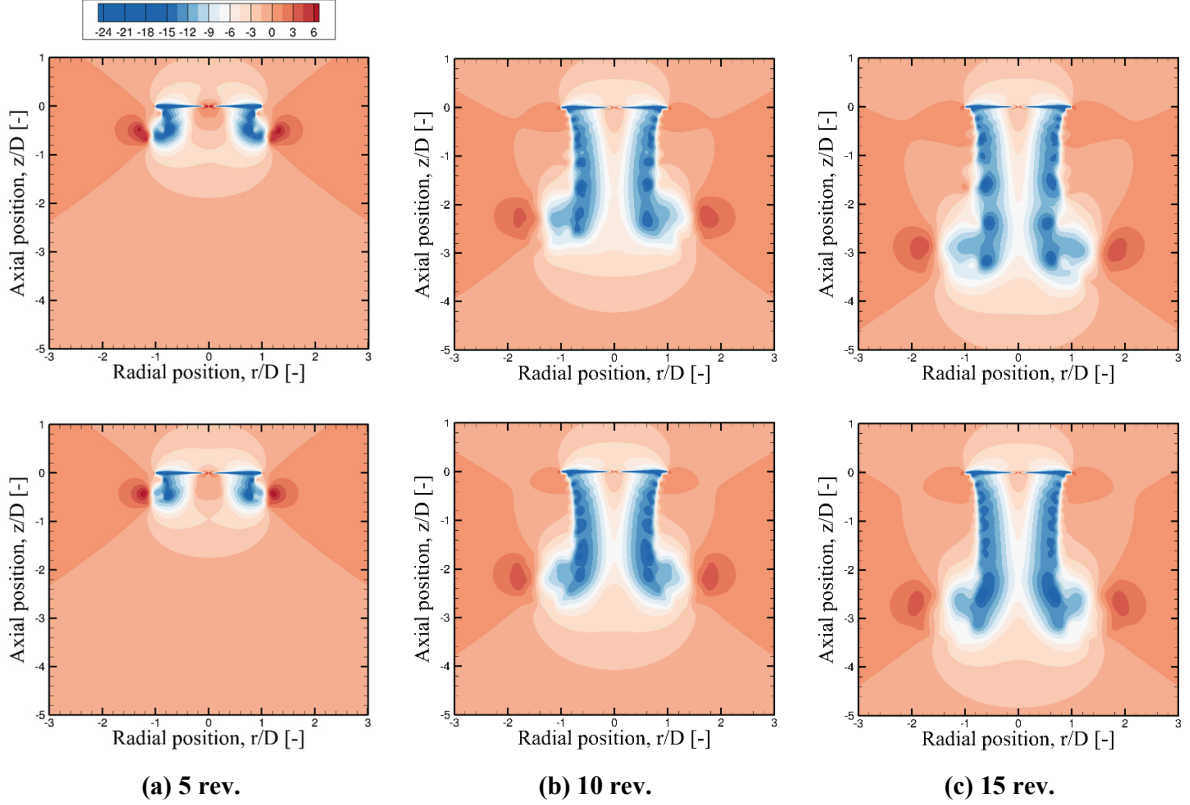
Fig. 7 Comparison of evolution of wake-induced velocity fields predicted by VPM simulations with FMM (top) and direct (bottom) methods.

4.3 Wake structure

The evolution of unsteady wake geometries behind the rotor with the aid of the vorticity fields is shown in Fig. 8 for the case of $\theta_{75} = 10.75°$. With increases in revolutions of the OH-13E rotor, the contours of vorticity magnitude on a vertical cross-section (x–z plane) across the center of the rotating axis were compared for FMM and direct simulations. The vorticity contour plots clearly show periodic shedding of wake vortices behind the rotor plane in both instances. In the wake vortices, different colors indicate opposing directions of vorticity. Individual plots in the figure provide the identification of vortex structures, which are mostly made up of tip vortices and shear layers. The pressure differential at the blade tip generates pairs of tip vortices, while shear layers form by merging of boundary layers on the upper and lower sides of the blade [72]. Although all features of the wake were captured properly, there are small differences in wake structure and in the magnitude of the vorticity contours, especially at higher revolutions, as can be seen in Fig. 8(c).

(a) 5 rev.   **(b) 10 rev.**   **(c) 15 rev.**
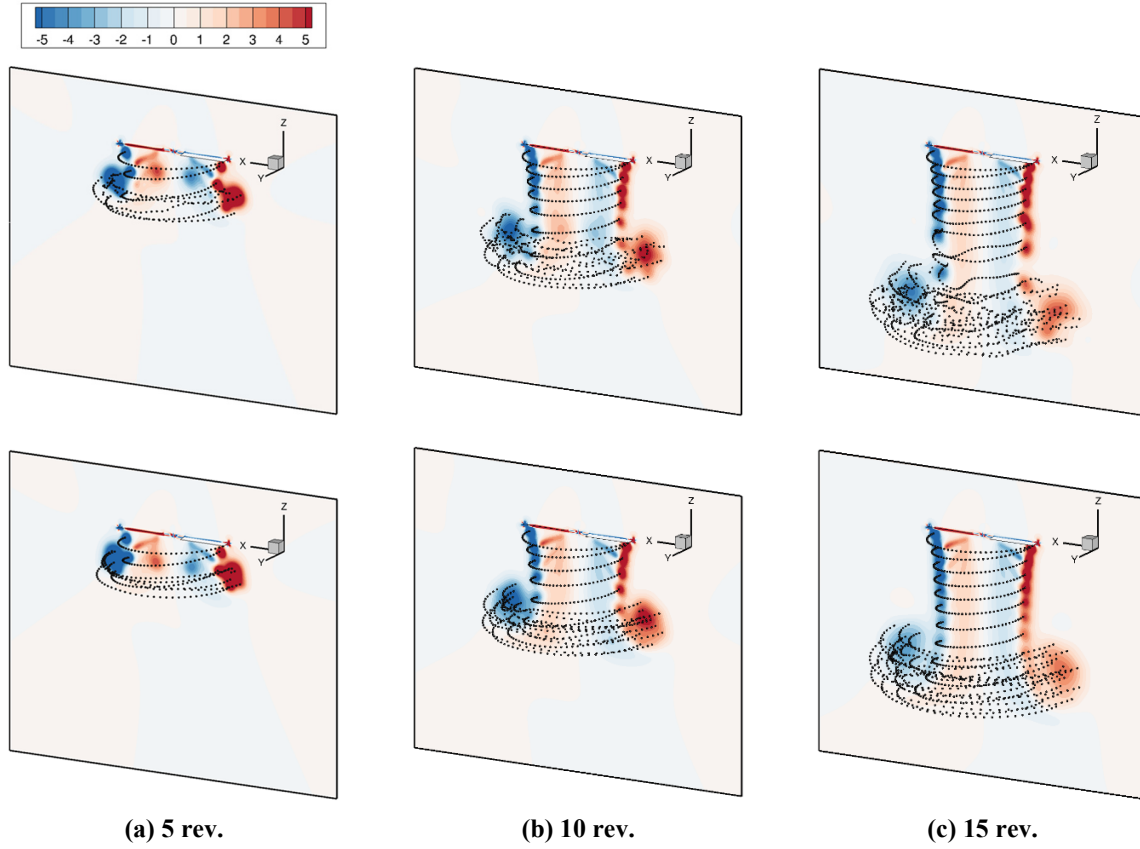
Fig. 8 Comparison of evolution of wake and vortical structures predicted by VPM simulations with FMM (top) and direct (bottom) methods.

Comparison of computational time for case 10.75º (θ_{75}) was performed as shown in Fig. 9. As was explained earlier, with the same given computational resources, FMM computation consumes more time for a smaller number of particles. Efficiency of FMM simulation was observed to be dramatically improved with a greater number of particles, as observed in Fig. 5. However, the computational time is dependent on not only the number of particles but also on their arrangement in space. Therefore, although the trend will remain similar irrespective of the type of simulation, the total computational time is a case-specific quantity. We evaluated the level of computational resources required by the direct method to match the simulation time by FMM. Each CPU has two threads. FMM computation was performed using ten threads and results were taken as a reference, as illustrated in Fig. 9. Direct simulation was executed by increasing the number of CPUs. It was observed that direct simulation required four times more computational resources than those required by FMM to match the time, as shown in Fig. 9.
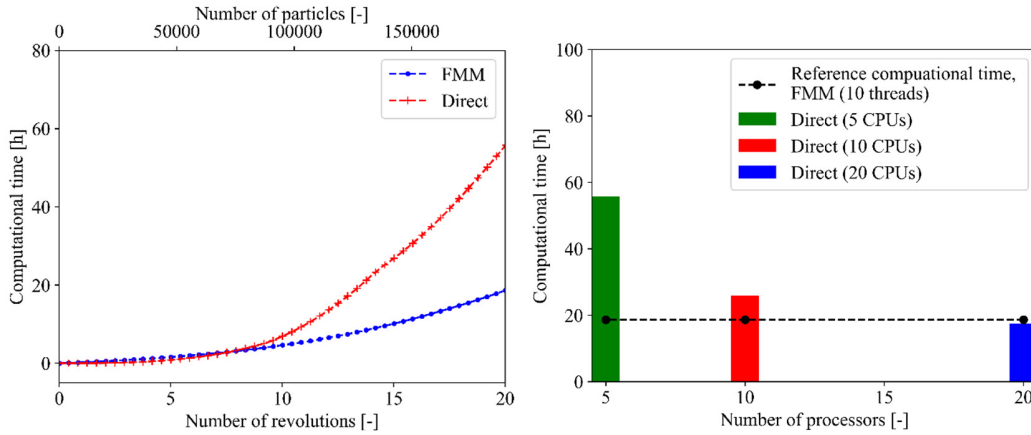
Fig. 9 Comparison of time profiling with respect to number of revolutions for FMM and direct computation.

5. Prediction of flow physics of multirotor

5.1 Multirotor model

One of the most well-known commercial UAV models is the DJI (Da Jiang Innovation) Phantom 2, which is the second generation of the company's Phantom RC aircraft. It has an X-shaped symmetric airframe and four rotors with connecting arms. The DJI Phantom 2 rotor is made up of tapered-twisted blades (DJI 9443 type); distributions of their chord and twist angles as a function of radial position were provided by Zawodny et al. [73]. That study provided geometric details on the DJI 9443 rotor blade, but sectional airfoil profiles were not provided. To retrieve these, digital high-resolution laser scanning was used. At the ends of the connecting arms, a two-bladed DJI 9443 with a diameter of 0.24 m (9.45 in.) was installed. The neighboring rotors were designed to rotate in the opposite direction to balance the angular moment and maintain the rotational attitude of the quadcopter. Viewed from above, one set of rotors rotated in a counter-clockwise (CCW) direction, and the other rotated in a clockwise (CW) direction.

Table 4 Model description of DJI quadrotor system [73]

Parameter	Value
Propeller model	DJI 9443
Number of rotors, N_R [-]	4
Number of blades, N_B [-]	2
Rotor diameter, D [m]	0.24
Rotational speed, Ω [RPM]	5400
Tip Mach number, M_{tip} [-]	0.2

The parameters used in the present study are listed in Table 4. The separation distance between the rotors was fixed at *0.2D* (Here, *D* is rotor diameter) with hovering and the forward speed of 2.5 m/s and 5.0 m/s, respectively. Each rotor blade is represented in the numerical simulation by the distribution of quadrilateral vortex ring elements on the camber surface in the chordwise and spanwise directions. Each blade's surface grid resolution is 30 chordwise by 40 spanwise, and the quadcopter's computations are performed at a rotational speed of 5400 rpm. Two planes Y+ and Y-, as shown in Fig. 10, are used to represent the flowfield in the forward flight condition.
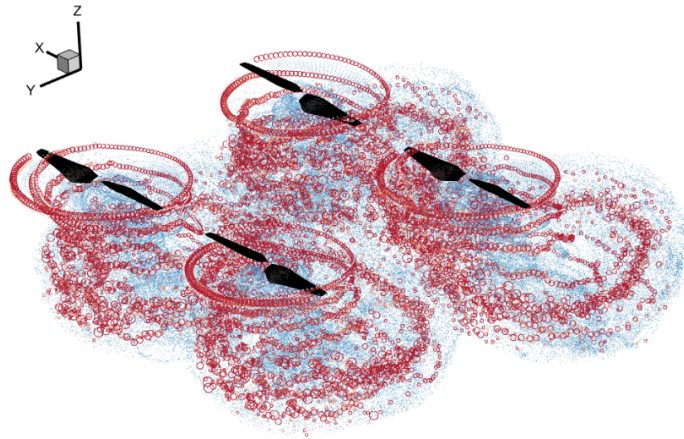
Fig. 10 Wake structure of multirotor configuration in forward flight

In this study, we compared the average thrust coefficients in both hovering and forward flight conditions using our algorithm, referred to as the FMM, with the direct method, as illustrated in Fig. 11. This direct method algorithm was previously employed by Lee et al. [61] for calculating the aerodynamics and acoustics of a quadrotor configuration.

We validated our FMM approach against this direct method. The highest discrepancy noted was approximately 2.5% during hovering, compared to the direct method. Consequently, the error margin of our method is relatively negligible in relation to the direct method.
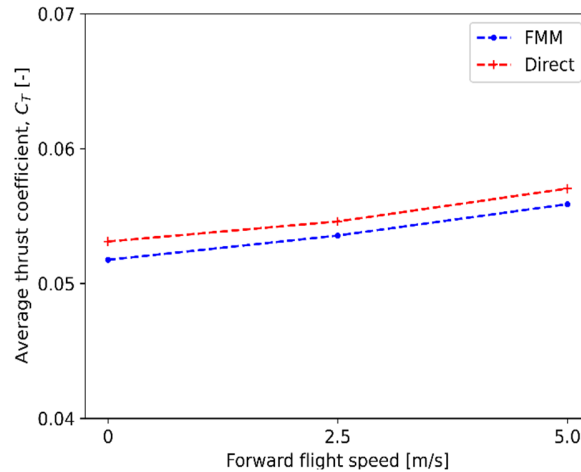
Fig. 11 Comparison of the averaged thrust coefficients of multirotor configuration in hover and forward flight conditions between FMM and direct computation.

5.2 Hover flight

The evolution of wake-induced downwash with respect to revolutions, as predicted by FMM and direct methods, is illustrated in Fig. 12 for a hovering quadrotor system. Due to high rotor-rotor interaction, the multipole order required for the quadrotor system was set at 10 to achieve accurate results. The instantaneous axial velocity along the induced flow direction presented here can be used to understand how rotor-to-rotor interactions affect the flow structures behind the multirotor system. As can be seen in Fig. 12(a), the velocity contours behind the isolated rotor were found to be axially symmetric and circular, with strong axial convection and radial contraction of wake flow observed by both direct and FMM methodology. Very slight variation was observed in the flow structures when comparing the contours of downwash velocity using the FMM and direct approach on a vertical cross-section (x-z plane) over the center of the rotating axis (see Fig. 12(a)). Both the FMM and the direct approach can capture the periodic shedding of wake vortices behind the rotor plane under all circumstances.
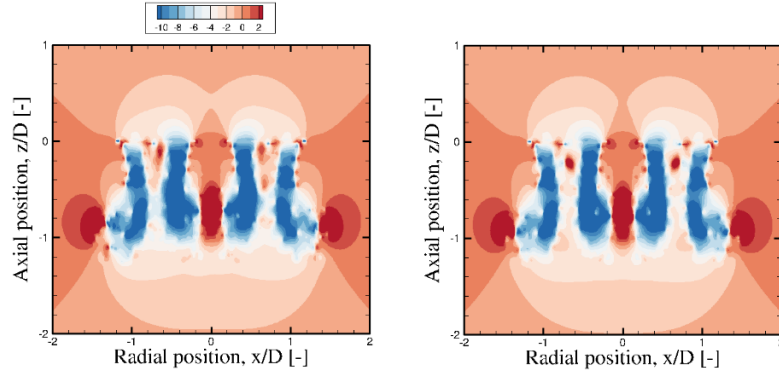
(a) Wake-induced downwash
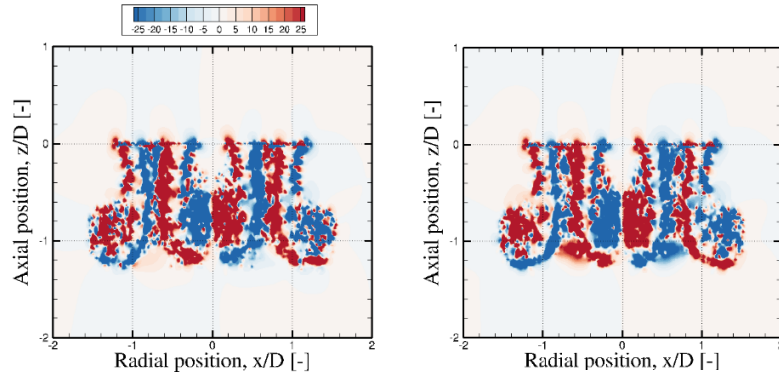
(b) Vortical structure

Fig. 12 Comparison of wake-induced downwash and vortical structure predicted by VPM simulations with FMM (left) and direct (right) methods.

To further investigate the development of unsteady wake geometries behind the multirotor along the induced flow direction, and to better understand the effect of rotor interaction on the vorticity structure, the vorticity fields were studied as shown in Fig. 12(b). Different colors imply opposite directions of vorticity in the wake vortices. The individual plots in Fig. 12 help in locating the various vortex formations, which are mostly made up of tip vortices and shear layers. Pairs of tip vortices are generated due to pressure differences at the blade tip, while shear layers develop by merging of boundary layers on the upper and lower surfaces of the blade. Coherent vortical structures begin to emerge in the vicinity of the wake, but, with the progress of rotation, these become distorted due to the presence of subsequent tip vortices trailing from the nearby rotors. The periodic shedding of wake vortices behind the rotor plane can be easily observed by FMM and direct methods, as shown in Fig. 12(a) and Fig. 12(b), by comparing contours of vorticity magnitude on an x-z vertical cross-section plane through the center of the rotating axis.

5.3 Forward flight

The quadrotor system was simulated for forward flight velocities of 2.5 m/s and 5.0 m/s, respectively, with both FMM and direct methodologies. The results for each quantity, such as downwash velocity and vorticity, are presented and compared with respect to forward speed and cutting plane (Y+ and Y-), as shown in Fig. 10. The Y+ plane is defined as the plane going through the rotor system in the perpendicular direction for rotors first encountering the free stream velocity; the Y- plane is for the rotors downstream of the upstream rotors. The downwash velocity values on the Y+ plane for forward flight speeds of 2.5 m/s and 5.0 m/s are shown in Fig. 13(a) and 13(b). An interesting observation that was made during the study was that at low forward speed, wake interaction was higher at the Y+ plane than at the high forward speed, whereas at high forward speed, wake interaction was higher at the Y- plane than at the low forward speed with the progress of rotor revolution. Compared to the high forward speed, at a lower forward speed, the wake can travel a greater distance in the axial direction (Fig. 13) due to low convection velocity. At low forward speed, with increases in rotation, wakes that emanated long ago detached themselves from wakes that emanated recently from the rotor. The convection velocity had a dominant effect over the rotor effect for high forward speed, and no considerable change was observed in the downwash velocity field with increase in rotation of rotor. The downwash velocity values at the Y+ plane for the forward speeds of 2.5 m/s and 5.0 m/s were compared using FMM and direct methods. Differences in the field were observed to be negligible even when rotor-rotor wake interaction increased with increases in forward speed and number of revolutions.
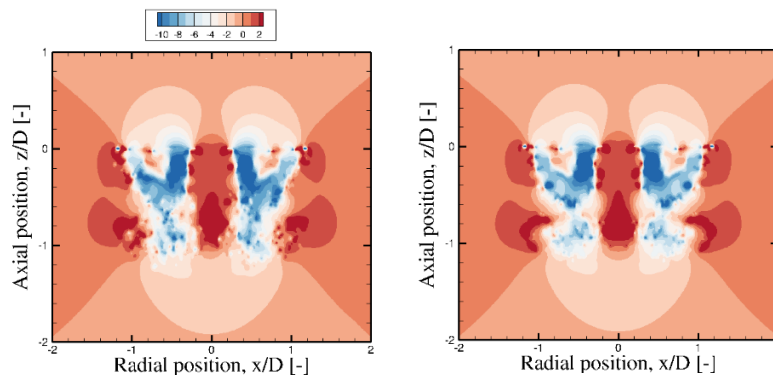
(a) Forward velocity of 2.5 m/s
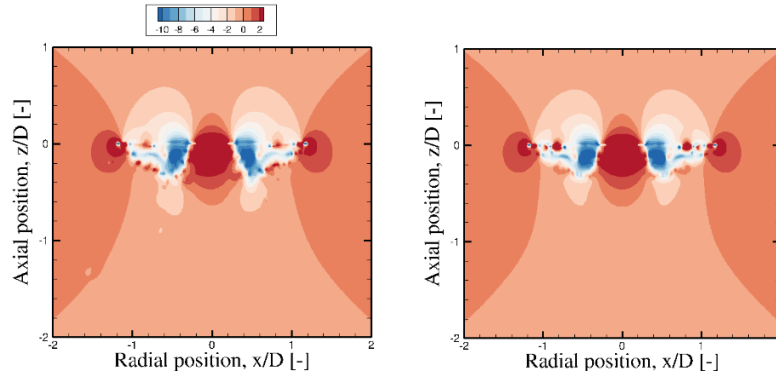
(b) Forward velocity of 5.0 m/s

Fig. 13 Comparison of wake-induced downwash predicted by VPM simulations with FMM (left) and direct (right) methods at upstream location (+Y).

The downwash velocity field was next compared for the Y- plane using FMM and direct methodology for forward speeds of 2.5 m/s and 5.0 m/s, respectively. The wake interaction significantly increased in the Y- plane for both cases of forward flight, as shown in Fig. 14. Rotor-rotor wake interaction was observed to be highest for the forward speed of 5.0 m/s at the highest rotation, as shown in Fig. 14. In the case of high-speed forward flight, due to high convection velocity, wakes emanating from the upstream rotors interacted intensely with downstream rotor wakes, causing greater wake interaction than that of low-speed forward flight. Movements of wakes in the Y- plane in the axial direction were observed to be similar in both cases.

Comparison of FMM and direct methods for both cases of forward flight conditions showed small differences in downwash at higher revolutions, as shown in Fig. 14. It was also observed that the symmetric pattern with respect to the center line passing through the rotor system was distorted in the case of FMM due to the high degree of particle interaction from different rotors. Prediction accuracy can be increased by increasing the order of multipole in FMM, but that incurs an increase in computational time, so it is necessary rather to balance the accuracy and computation time so that there is good agreement between integrated quantities (such as thrust coefficient) between both methods
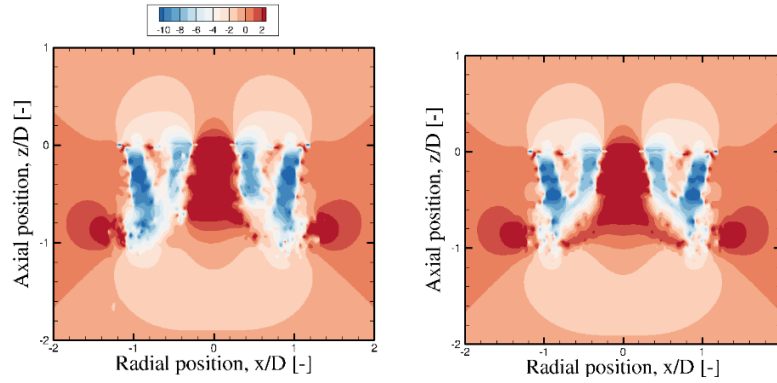
(a) Forward velocity of 2.5 m/s
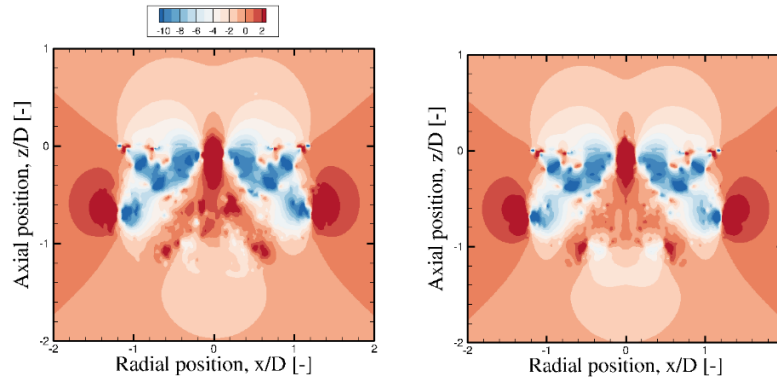
(b) Forward velocity of 5.0 m/s

Fig. 14 Comparison of wake-induced downwash predicted by VPM simulations with FMM (left) and direct (right) methods at downstream location (-Y).

The vorticity fields wee defined in order to better understand the evolution of unsteady wake geometries behind the multirotor along the Y+ and Y- planes, as shown in Fig.15. We first compared the vorticity field with respect to the forward speed of the system on the Y+ plane and then on Y- plane. The vorticity contour plots show periodical shedding of wake vortices behind the rotor plane. Different colors indicate opposite directions of vorticity in the wake vortices. The individual figures show the vortex structures, which are mostly made up of tip vortices and shear layers. The pressure difference at the blade tip generates pairs of tip vortices, and shear layers are formed by merging of boundary layers on the upper and lower surfaces of the blade.
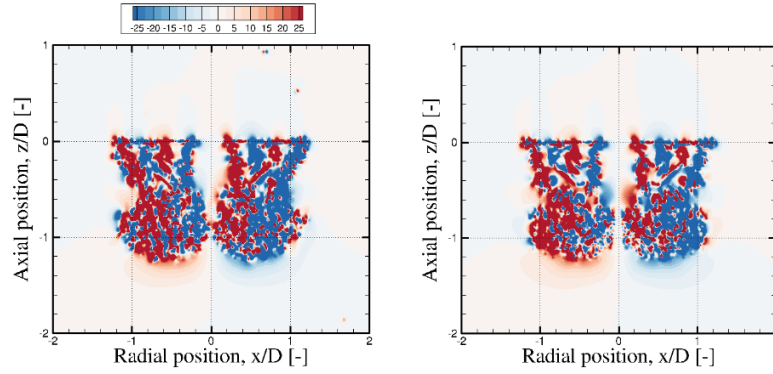
(a) Forward velocity of 2.5 m/s
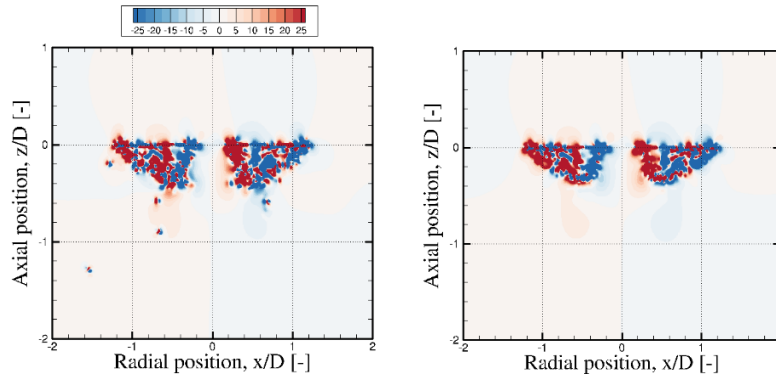
(b) Forward velocity of 5.0 m/s

Fig. 15 Comparison of vortical structure predicted by VPM simulations with FMM (left) and direct (right) methods at upstream location (+Y).

At the center of the vehicle, with progress of the revolution of the rotors, the wake vortices interact severely with each other, as was observed in hovering and at low forward speed. The phenomenon of higher interaction in the case of low forward speed at the Y+ plane is also evident from the vorticity contours shown in Fig. 15(a); however, for high forward speed, no significant wake interaction was observed, as shown in Fig. 15(b). The rotor-rotor wake interaction increased with the progress of the revolution of the rotor. Due to the low free stream convection velocity, the wake moved more in the axial direction at low forward speed than at high forward speed. The vorticity field obtained from FMM computation was observed to be almost identical to the vorticity field obtained from direct computation.
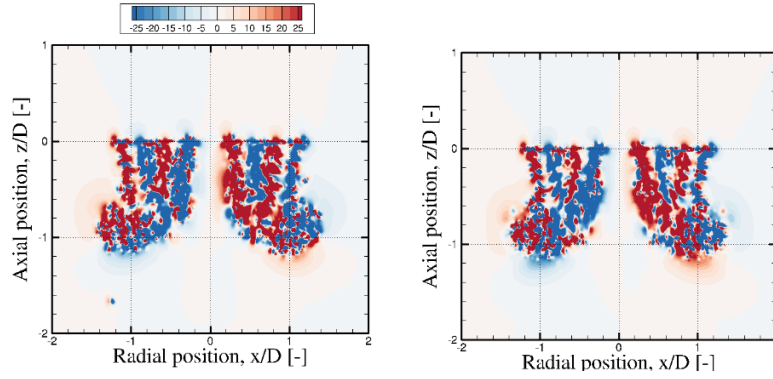
(a) Forward velocity of 2.5 m/s
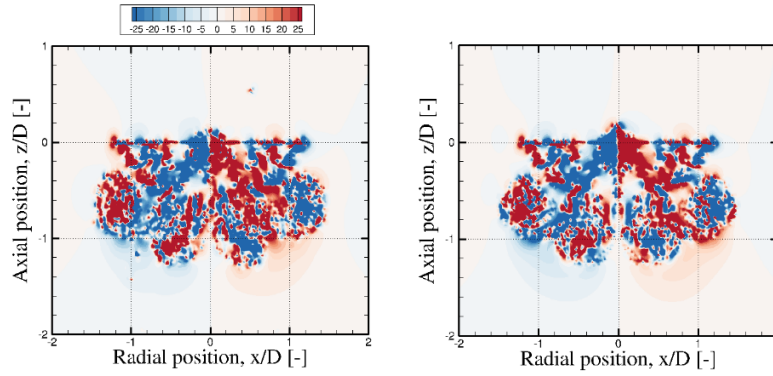
(b) Forward velocity of 5.0 m/s

Fig. 16 Comparison of vortical structure predicted by VPM simulations with FMM (left) and direct (right) methods at downstream location (-Y).

The vorticity field was compared on the Y- plane for both forward speed cases with FMM and direct methodology. As can be observed in the downwash plots, rotor-rotor wake interaction was higher for high forward flight speed than for low forward flight speed, as shown in Fig. 14; the same pattern can be seen in the vorticity plots, as well as in Fig. 16. With the progress of revolutions, wake interaction was observed to increase dramatically in the case of high forward flight, as can be seen in Fig. 16(b). Although a large degree of rotor-rotor wake interaction was observed, the results obtained from FMM showed only insignificant differences when compared with those of the direct method in both cases of forward flight, as shown in Fig. 16.

The advantage of FMM can be clearly observed when the number of particles is sufficiently large. The computational efficiency was observed in cases of C-T rotor and OH-13E rotor, with results shown in Fig. 4 and Fig. 9, respectively. In both cases, there was one rotor, and the number of particles emanating from the rotor was not

sufficiently large. Therefore, for the initial few revolutions, the direct method required more computational time than did FMM. Once the cut-off number of particles was reached, FMM showed its full potential in computational efficiency. Comparison of time profiling in a typical quadrotor case is shown in Fig. 17. The trend of the time profiling plot does not change for hovering or any forward flight case because the numbers of particles emanated in all cases were the same. The quadrotor case produced a large number of particles to describe its flowfield; this number increased with the progress of rotor revolutions. The plot below compares computational time per processor with respect to revolutions and number of particles. Because the number of particles continuously increased with the progress of the revolutions, the computational time required by the direct method increased exponentially; in contrast, the time consumed by FMM did not show any significant increase.
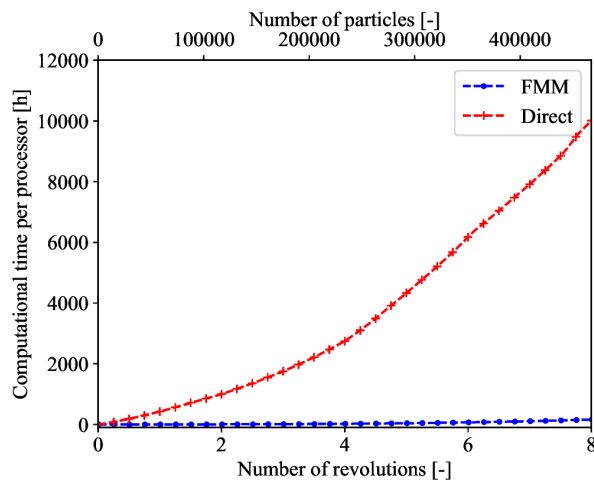
Fig. 17 Comparison of time profiling per processor with respect to number of revolutions for FMM and direct computation.

6. Conclusions

The present work described a complete and versatile investigation of the aerodynamic and wake dynamics of two different kinds of rotors and then applied the methodology to a quadrotor system. The purpose of this research was to look at the effects on aerodynamic forces, tip vortex trajectory, wake structure, and downwash velocity using calculations by FMM and the direct method of induced velocity of vortex particles. In this work, aerodynamic performance and wake dynamics were predicted using a coupling of the NVLM and VPM algorithms. Comparison of

aerodynamic forces along with wake structure and vorticity field was the primary focus of the present investigation. The following is a summary of our findings:

1) Because this is an approximate method, the order of accuracy of FMM can be increased by applying a higher-order polynomial. However, an intelligent choice must be made because, beyond a certain order, improvements in accuracy are not justifiable with respect to computational time. Therefore, different flow features are addressed in this investigation. It was also found that differences in flow features have small effects on prediction of important parameters such as aerodynamic forces, tip vortex trajectory, wake structure, downwash velocity, etc.

2) The main motivation for adopting FMM in the Lagrangian framework is not only a reduction in computational time but also a reduction of computational resources. This study investigated differences in computational time for certain given computational resources and showed excellent outcomes. The number of processors in direct computation was increased until the computational time when using FMM became approximately equal to that of the direct method. For one particular case, it was observed that the computational resources required for the direct method were four times those necessary in the FMM to achieve the same computational time. It should nonetheless be noted that there is variation in time profiling depending on the number and distribution of the particles. The computational cost of a full simulation, up to stabilization of the thrust coefficient with respect to the number of revolutions and wake particles, was investigated and reported; this information will be beneficial for design engineers.

The recent surge in on research of UAM aerodynamics for multirotor configurations motivated the authors to scrutinize the applicability of FMM in terms of both accuracy and computational resources. The flow field in the multirotor system is complex because of interaction of wakes from different rotors and interactions between wakes and fuselage. Accurate calculation of aerodynamic forces and aeroacoustics is directly related to accuracy in computation of wake structure. Although the direct method is accurate, it becomes too expensive, especially in multirotor configuration. Therefore, implementation of FMM becomes a necessity, especially in multirotor systems. Even though it delivers only approximate solutions, FMM is sufficiently accurate to correctly mimic the overall system behavior.

In the present work, we have chosen two benchmark rotor experiments, namely Caradonna Tung and OH-13E; we have shown the applicability of FMM to the complex flow field and investigated its differences in flow features

compared with those of the direct method. In addition, the methodology was applied to a quadrotor system at different forward flight speeds, and the flowfield physics was explored to investigate differences between direct and FMM methods in a complex, highly spatial inhomogeneous flowfield.

References

[1]   K. Song, H. Yeo, J.-H. Moon, Approach Control Concepts and Optimal Vertiport Airspace Design for Urban Air Mobility (UAM) Operation, Int J Aeronaut Sp Sci, 22 (2021) 982–994.

[2]   B.T. Park, H. Kim, S.H. Kim, Vertiport Performance Analysis for On-Demand Urban Air Mobility Operation in Seoul Metropolitan Area, Int J Aeronaut Sp Sci, 23 (2022) 1065–1078.

[3]   J.-Y. An, Y.-S. Choi, I.-R. Lee, M. Lim, C.-J. Kim, Performance Analysis of a Conceptual Urban Air Mobility Configuration Using High-Fidelity Rotorcraft Flight Dynamic Model, Int J Aeronaut Sp Sci, (2023).

[4]   M.E. Kelly, K. Duraisamy, R. Brown, Predicting blade vortex interaction, airloads and acoustics using the vorticity transport model, in: 9th Am Helicopter Soc Aeromechanics Spec Meet, 2008.

[5]   T. Renaud, A. Le Pape, S. Péron, Numerical analysis of hub and fuselage drag breakdown of a helicopter configuration, CEAS Aeronaut J, 4 (2013) 409–419.

[6]   T.C.A. Stokkermans, D. Usai, T. Sinnige, L.L.M. Veldhuis, Aerodynamic Interaction Effects Between

Propellers in Typical eVTOL Vehicle Configurations, J Aircr, 58 (2021) 815–833.

[7] U. Saetti, J.F. Horn, K.S. Brentner, W. Villafana, D.A. Wachspress, Rotorcraft simulations with coupled flight dynamics, free wake, and acoustics, in: 72nd Am Helicopter Soc Int Annu Forum 2016, West Palm Beach, 2016: pp. 2226–2237.

[8] J. Ko, J. Kim, V. Saravanan, S. Lee, Noise Sources and Spectral Characteristics of the Tip-Jet Driven Rotor, Int J Aeronaut Sp Sci, 22 (2021) 33–41.

[9] Z. Jia, S. Lee, Impulsive loading noise of a lift-offset coaxial rotor in high-speed forward flight, AIAA J, 58 (2020) 687–701.

[10] Z. Jia, S. Lee, Aerodynamically induced noise of a lift-offset coaxial rotor with pitch attitude in high-speed forward flight, J Sound Vib, 491 (2021) 115737.

[11] N.M. Komerath, M.J. Smith, C. Tung, A review of rotor wake physics and modeling, J Am Helicopter Soc, 56 (2011) 22006.

[12] G. Iosilevskii, Y. Levy, Experimental and numerical study of cyclogiro aerodynamics, AIAA J, 44 (2006) 2866–2870.

[13] D. Shukla, N. Hiremath, N.M. Komerath, Low Reynolds Number Aerodynamics Study on Coaxial and Quad-Rotor, in: 2018 Appl Aerodyn Conf, American Institute of Aeronautics and Astronautics, Atlanta, Georgia, 2018.

[14] M. Veismann, M. Gharib, High Fidelity Aerodynamic Force Estimation for Multirotor Crafts in Free Flight, in: AIAA Scitech 2020 Forum, American Institute of Aeronautics and Astronautics, Orlando, Florida, 2020.

[15] D. Linton, R. Widjaja, B. Thornber, Actuator Surface Model with Computational-Fluid-Dynamics-Convected Wake Model for Rotorcraft Applications, AIAA J, 59 (2021) 2935–2949.

[16] R. Narducci, Hover Performance Assessment of Several Tip Shapes using OVERFLOW, in: 53rd AIAA Aerosp Sci Meet, American Institute of Aeronautics and Astronautics, 2015.

[17] N.M. Chaderjian, Navier-Stokes simulation of UH-60A rotor/wake interaction using adaptive mesh refinement, in: Proc 73rd Annu Forum Am Helicopter Soc, Fort Worth, Texas, 2017.

[18] C. Pang, H. Yang, Z. Gao, S. Chen, Enhanced adaptive mesh refinement method using advanced vortex identification sensors in wake flow, Aerosp Sci Technol, 115 (2021) 106796.

[19] Y. Seo, Y. Hong, K. Yee, Numerical Investigation of Wing–Multiple Propeller Aerodynamic Interaction

Using Actuator Disk Method, Int J Aeronaut Sp Sci, 23 (2022) 805–822.

[20]   I.C. Wilbur, A. Moushegian, M.J. Smith, G.R. Whitehouse, UH-60A Rotor Analysis with an Accurate Dual-Formulation Hybrid Aeroelastic Methodology, J Aircr, 57 (2020) 113–127.

[21]   S. Yoon, P.V. Diaz, D.D. Boyd Jr, W.M. Chan, C.R. Theodore, Computational aerodynamic modeling of small quadcopter vehicles, in: Am Helicopter Soc 73rd Annu Forum Fort Worth, Texas, 2017.

[22]   J.G. Leishman, S. Ananthan, Aerodynamic Optimization of a Coaxial Proprotor, Am Helicopter Soc 62nd Annu Forum, Phoenix, USA, (2006).

[23]   S.Y. Wie, S. Lee, D.J. Lee, Potential Panel and Time-Marching Free-Wake-Coupling Analysis for Helicopter Rotor, J Aircr, 46 (2009) 1030–1041.

[24]   M. Gennaretti, G. Bernardini, J. Serafini, G. Romani, Rotorcraft comprehensive code assessment for blade–vortex interaction conditions, Aerosp Sci Technol, 80 (2018) 232–246.

[25]   Y. Crispin, Unsteady rotor aerodynamics using a vortex panel method, in: 9th Atmos Flight Mech Conf, American Institute of Aeronautics and Astronautics, 1982.

[26]   N. Hariharan, L. Sankar, A review of computational techniques for rotor wake modeling, in: 38th Aerosp Sci Meet Exhib, American Institute of Aeronautics and Astronautics, Reno, NV, 2000.

[27]   J. Katz, A. Plotkin, Low-speed aerodynamics, Cambridge university press, 2001.

[28]   H. Lee, Development of nonlinear vortex lattice method for predicting wind turbine performance and wake structures, Korea Advanced Institute of Science and Technology, 2019.

[29]   M.J. Bhagwat, J.G. Leishman, Generalized viscous vortex model for application to free-vortex wake and aeroacoustic calculations, in: Proc 58th Annu Forum Am Helicopter Soc Helicopter Soc, American Helicopter Society, Inc, 2002: pp. 2042–2057.

[30]   D.J. Lee, Numerical prediction of rotor tip-vortex roll-up in axial flights by using a time-marching free-wake method, in: Vor Methods, World Scientific, 2000: pp. 177–187.

[31]   D.J. Lee, S.U. Na, Numerical simulations of wake structure generated by rotating blades using a time marching, free vortex blob method, Eur J Mech - B/Fluids, 18 (1999) 147–159.

[32]   J. Barnes, P. Hut, A hierarchical O(N log N) force-calculation algorithm, Nature, 324 (1986) 446–449.

[33]   D.J. Willis, J. Peraire, J.K. White, A combined pFFT-multipole tree code, unsteady panel method with vortex particle wakes, Int J Numer Methods Fluids, 53 (2007) 1399–1422.

[34] I. Lashuk, A. Chandramowlishwaran, H. Langston, T.-A. Nguyen, R. Sampath, A. Shringarpure, R. Vuduc, L. Ying, D. Zorin, G. Biros, A massively parallel adaptive fast-multipole method on heterogeneous architectures, in: Proc Conf High Perform Comput Networking, Storage Anal, 2009: pp. 1–12.

[35] E. Ryatina, A. Lagno, The Barnes—Hut-type algorithm in 2D Lagrangian vortex particle methods, in: J Phys Conf Ser, IOP Publishing, 2021: p. 12069.

[36] E.J. Alvarez, A. Ning, High-Fidelity Modeling of Multirotor Aerodynamic Interactions for Aircraft Design, AIAA J, 58 (2020) 4385–4400.

[37] L. Greengard, V. Rokhlin, A fast algorithm for particle simulations, J Comput Phys, 73 (1987) 325–348.

[38] L. Greengard, The rapid evaluation of potential fields in particle systems, MIT press, Cambridge, MA, 1988.

[39] H. Cheng, L. Greengard, V. Rokhlin, A fast adaptive multipole algorithm in three dimensions, J Comput Phys, 155 (1999) 468–498.

[40] L. Ying, G. Biros, D. Zorin, A kernel-independent adaptive fast multipole algorithm in two and three dimensions, J Comput Phys, 196 (2004) 591–626.

[41] S. DENG, C. JIANG, Y. WANG, H. WANG, Acceleration of unsteady vortex lattice method via dipole panel fast multipole method, Chinese J Aeronaut, 34 (2021) 265–278.

[42] F. Thönnißen, E.K. Fritz, W. Schröder, Acceleration of vortex-particle simulations using a pseudo-particle method, in: J Phys Conf Ser, IOP Publishing, 2020: p. 52006.

[43] M. Vines, B. Houston, J. Lang, W.-S. Lee, Vortical inviscid flows with two-way solid-fluid coupling, IEEE Trans Vis Comput Graph, 20 (2013) 303–315.

[44] W. Fong, E. Darve, The black-box fast multipole method, J Comput Phys, 228 (2009) 8712–8725.

[45] A. van Garrel, C.H. Venner, H.W. Hoeijmakers, Fast multilevel panel method for wind turbine rotor flow simulations, in: 35th Wind Energy Symp, 2017: p. 2001.

[46] A. Van Garrel, Development of a wind turbine aerodynamics simulation module, (2003).

[47] J. Tan, H. Wang, Simulating unsteady aerodynamics of helicopter rotor with panel/viscous vortex particle method, Aerosp Sci Technol, 30 (2013) 255–268.

[48] W. Zhu, M. Morandini, S. Li, Viscous Vortex Particle Method Coupling with Computational Structural Dynamics for Rotor Comprehensive Analysis, Appl Sci, 11 (2021).

[49] E.J. Alvarez, A. Ning, Modeling Multirotor Aerodynamic Interactions Through the Vortex Particle Method,

in: AIAA Aviat 2019 Forum, American Institute of Aeronautics and Astronautics, Dallas, Texas, 2019.

[50]   J. Zhao, C. He, A viscous vortex particle model for rotor wake and interference analysis, J Am Helicopter Soc, 55 (2010) 12007.

[51]   C. Crozon, R. Steijl, G.N. Barakos, Coupled flight dynamics and CFD – demonstration for helicopters in shipborne environment, Aeronaut J, 122 (2018) 42–82.

[52]   V. Proulx-Cabana, M.T. Nguyen, S. Prothin, G. Michon, E. Laurendeau, A Hybrid Non-Linear Unsteady Vortex Lattice-Vortex Particle Method for Rotor Blades Aerodynamic Simulations, Fluids, 7 (2022) 81.

[53]   F. Rovere, G. Barakos, R. Steijl, Safety analysis of Rotors In Ground Effect, in: AIAA Aviat 2021 FORUM, American Institute of Aeronautics and Astronautics, 2021.

[54]   R. Singh, H. Kang, J. Sirohi, Computational Investigations of Transient Loads and Blade Deformations on Coaxial Rotor Systems, in: 33rd AIAA Appl Aerodyn Conf, American Institute of Aeronautics and Astronautics, 2015.

[55]   A. Datta, J. Sitaraman, I. Chopra, J.D. Baeder, CFD/CSD prediction of rotor vibratory loads in high-speed flight, J Aircr, 43 (2006) 1698–1709.

[56]   M.J. Bhagwat, J.G. Leishman, Stability analysis of helicopter rotor wakes in axial flight, J Am Helicopter Soc, 45 (2000) 165–178.

[57]   F.X. Caradonna, C. Tung, Experimental and analytical studies of a model helicopter rotor in hover, (1981) NASA-TM-81232.

[58]   D.W. Boatwright, Measurements of velocity components in the wake of a full-scale helicopter rotor in hover, U.S. Army Air Mobility Research and Development Lab., Fort Eustis, VA, 1972.

[59]   H. Lee, D.-J. Lee, Effects of platform motions on aerodynamic performance and unsteady wake evolution of a floating offshore wind turbine, Renew Energy, 143 (2019) 9–23.

[60]   H. Lee, D.-J. Lee, Wake impact on aerodynamic characteristics of horizontal axis wind turbine under yawed flow conditions, Renew Energy, 136 (2019) 383–392.

[61]   H. Lee, D.-J. Lee, Rotor interactional effects on aerodynamic and noise characteristics of a small multirotor unmanned aerial vehicle, Phys Fluids, 32 (2020) 47107.

[62]   H. Lee, D.-J. Lee, Numerical investigation of the aerodynamics and wake structures of horizontal axis wind turbines by using nonlinear vortex lattice method, Renew Energy, 132 (2019) 1121–1133.

[63] G.S. Winckelmans, A. Leonard, Contributions to vortex particle methods for the computation of three-dimensional incompressible unsteady flows, J Comput Phys, 109 (1993) 247–273.

[64] G.S. Winckelmans, Topics in vortex methods for the computation of three-and two-dimensional incompressible unsteady flows, California Institute of Technology, 1989.

[65] L. Ying, G. Biros, D. Zorin, H. Langston, A new parallel kernel-independent fast multipole method, in: SC'03 Proc 2003 ACM/IEEE Conf Supercomput, IEEE, 2003: p. 14.

[66] W.B. March, B. Xiao, S. Tharakan, C.D. Yu, G. Biros, A kernel-independent FMM in general dimensions, in: SC '15 Proc Int Conf High Perform Comput Networking, Storage Anal, 2015: pp. 1–12.

[67] L. Ying, A kernel independent fast multipole algorithm for radial basis functions, J Comput Phys, 213 (2006) 451–457.

[68] D. Malhotra, G. Biros, PVFMM: A Parallel Kernel Independent FMM for Particle and Volume Potentials, Commun Comput Phys, 18 (2015) 808–830.

[69] C. He and Jinggen Zhao, Modeling rotor wake dynamics with viscous vortex particle method, AIAA Journal2, 47 (2009) 902–915.

[70] A. Gholami, D. Malhotra, H. Sundar, G. Biros, FFT, FMM, or multigrid? A comparative study of state-of-the-art Poisson solvers for uniform and nonuniform grids in the unit cube, SIAM J Sci Comput, 38 (2016) C280–C306.

[71] A. Kebbie-Anthony, N.A. Gumerov, S. Preidikman, B. Balachandran, S. Azarm, Fast multipole accelerated unsteady vortex lattice method based computations, J Aerosp Inf Syst, 16 (2019) 237–248.

[72] T.J. Mueller, J.D. DeLaurier, Aerodynamics of small vehicles, Annu Rev Fluid Mech, 35 (2003) 89–111.

[73] N.S. Zawodny, D.D. Boyd Jr, C.L. Burley, Acoustic characterization and prediction of representative, small-scale rotary-wing unmanned aircraft system components, in: Am Helicopter Soc 72nd Annu Forum Technol Disp, Florida, USA, 2016.